

Time-dependent phase matching of high-order-harmonic generationFeng Wang,¹ Lixin He,¹ Chunyang Zhai,¹ Wenjing Shi,¹ Qingbin Zhang,¹ Pengfei Lan,^{1,*} and Peixiang Lu^{1,2,†}¹*School of Physics and Wuhan National Laboratory for Optoelectronics, Huazhong University of Science and Technology, Wuhan 430074, China*²*Laboratory of Optical Information Technology, Wuhan Institute of Technology, Wuhan 430205, China*

(Received 2 November 2015; published 28 December 2015)

We theoretically investigate the influence of time-dependent phase matching on high-order-harmonic generation (HHG). The results show that the phase-matching degrees of the short and long paths are different at the leading and falling edges of the driving laser pulse. By using the strong-field approximation model and solving the Maxwell equations, we demonstrate that the time-dependent phase matching leads to the harmonic splitting with either a blue- or a red-frequency shift in the HHG spectra. Moreover, we also discuss the influence of the laser intensity, the laser duration, and the position of the gas medium on the time-dependent phase matching as well as the spatial and spectral properties of the HHG spectra.

DOI: [10.1103/PhysRevA.92.063839](https://doi.org/10.1103/PhysRevA.92.063839)

PACS number(s): 42.65.Ky, 42.65.Re, 32.80.Rm, 42.50.Hz

I. INTRODUCTION

When intense laser pulses interact with atoms and molecules, high-order harmonics can be generated [1]. In recent years, high-order-harmonic generation (HHG) has been a topic of great interest due to its potential applications for the production of coherent extreme ultraviolet (XUV) [2,3], soft x ray [4], and attosecond pulses [5]. These ultrashort pulses may serve as an important tool for detecting and controlling the ultrafast electronic dynamics inside atoms or molecules [6–8]. On the other hand, the high-order-harmonic spectra encode rich information of the target gas, which has been used to image the molecular structure [9,10] and dynamics [11].

On the single-atom level, the HHG process can be well understood by the three-step model [12], where the laser-atom interaction is separated into ionization, acceleration, and recombination steps. Such a process periodically occurs every half optical cycle of the laser field. In each half cycle, there are two dominant quantum paths, which are usually called the long and short paths. The return time of the long path is very close to a full period of the laser field, while that of the short path is less than half a laser period.

A knowledge of the single-atom dynamics is not sufficient to interpret the experimental phenomenon; it is necessary to take the effects of propagation and phase matching of HHG in the macroscopic medium into account. Numerous experimental and theoretical results [13–17] have demonstrated that the short and long paths prefer different phase-matching conditions: when the medium is positioned after the laser focus, the short path is more effectively phase matched. In contrast, when the medium is located before the focus, the short path is the dominant on axis. Whereas, as the spatial divergence of the harmonics increases, the contribution of the long paths becomes dominant [18–21]. Many applications based on the selection of a specific electron path have been achieved by controlling the phase-matching conditions, such as the attosecond pulse generation [22–24],

the time-resolved studies of electronic dynamics [25–27], and retrieving carrier-envelope phases from the half-cycle cutoffs [28]. On the other hand, in the HHG process, phase matching is usually coupled with the single-atom response, which can lead to complex spatial structures in the harmonic spectra, such as interference fringes [29,30] and harmonic splitting [31–33], etc. These spatial properties of harmonics provide rich information regarding the HHG process [34,35], but the physical origins of these complex structures are not satisfactorily clarified. In general, the conventional phase-matching model leaves out all the time-dependent effects, which would be limited to understand the influence of phase matching on these complex spatial structures. Since the HHG process is ultrafast in time and spatiotemporal coupling usually occurs in the generating medium [36,37], investigating the time-dependent phase matching is necessary to understand the complex structures in harmonic spectra.

In this paper, we theoretically investigate the effect of time-dependent phase matching on the generation of high-order harmonics driven by a 40-fs, 800-nm laser field in argon. It is shown that due to the ionization effect, the phase-matching degrees of the short and long paths are different at the leading and falling edges of the driving pulse. By using the strong-field approximation model and solving the Maxwell equations, we demonstrate that time-dependent phase matching leads to harmonic splitting with either a blue- or a red-frequency shift in the HHG spectra. We also discuss the influence of the laser intensity, laser duration, and position of the gas medium on time-dependent phase matching as well as the spatial and spectral properties of the HHG spectra. These results give a deeper insight and are beneficial for understanding the spatio-spectral features of HHG.

II. THEORETICAL MODEL

The nonlinear HHG process in atomic gases can be theoretically described by the single-atom response and the collective response of macroscopic gas to the laser and harmonic fields. In our calculation, we apply the strong-field approximation model (SFA) [38,39] to calculate the harmonic radiation. The time-dependent dipole momentum $d_n(t)$ (the

*pengfeilan@mail.hust.edu.cn

†lupeixiang@mail.hust.edu.cn

subscript nl stands for nonlinear) is described as

$$d_{nl}(t) = i \int_{-\infty}^t dt' \left[\frac{\pi}{\varepsilon + i(t-t')/2} \right]^{3/2} \times d^* [p_{st}(t',t) - A(t)] d [p_{st}(t',t) - A(t')] \times \exp[-iS_{st}(t',t)] E(t') g(t') + \text{c.c.}, \quad (1)$$

where $E(t)$ is the laser field, $A(t)$ is the corresponding vector potential, ε is a positive regularization constant, and p_{st} and S_{st} are the stationary momentum and quasiclassical action, respectively. Their values are

$$p_{st}(t',t) = \frac{1}{t-t'} \int_{t'}^t A(t'') dt'', \quad (2)$$

$$S_{st}(t',t) = (t-t')I_p - \frac{1}{2} p_{st}^2(t',t)(t-t') + \frac{1}{2} \int_{t'}^t A^2(t'') dt'', \quad (3)$$

where I_p is the ionization energy of the atom. $d(p)$ is the dipole matrix element for transitions from the ground state to the continuum state. In the continuum, the Coulomb effect of the parent ion on the electrons is ignored. The dipole element $d(p)$ is calculated by using the free-electron wave function (plane waves) to describe the continuum state. For hydrogenlike atoms, it can be expressed as

$$d(p) = i \frac{2^{7/2}}{\pi} (2I_p)^{5/4} \frac{p}{(p^2 + 2I_p)^3}. \quad (4)$$

The $g(t)$ in Eq. (1) represents the ground-state amplitude,

$$g(t) = \exp \left[- \int_{-\infty}^t w(t') dt' \right], \quad (5)$$

where $w(t)$ is the ionization rate, which is calculated by the Ammosov-Delone-Krainov (ADK) tunneling model [40],

$$w(t) = \omega_p |C_{n^*}|^2 \left(\frac{4\omega_p}{\omega_t} \right)^{2n^*-1} \exp \left(- \frac{4\omega_p}{3\omega_t} \right), \quad (6)$$

where

$$\omega_p = \frac{I_p}{\hbar}, \quad \omega_t = \frac{e|E_l(t)|}{\sqrt{2m_e I_p}}, \quad n^* = Z \left(\frac{I_{ph}}{I_p} \right)^{1/2},$$

$$|C_{n^*}|^2 = \frac{2^{2n^*}}{n^* \Gamma(n^* + 1) \Gamma(n^*)},$$

where Z is the net resulting charge of the atom, I_{ph} is the ionization potential of the hydrogen atom, and e and m_e are electron charge and mass, respectively. Then the harmonic spectrum is obtained by Fourier transforming the time-dependent dipole acceleration $a(t)$,

$$a_q = \frac{1}{T} \int_0^T a(t) \exp(-iq\omega t) dt, \quad (7)$$

where $a(t) = \ddot{d}_{nl}(t)$, and T and ω are the duration and frequency of the driving pulse, respectively. q corresponds to the harmonic order.

To simulate the collective response of macroscopic gas, we numerically solve the Maxwell wave equations for the fields of the laser pulse E_l and the harmonics E_h in cylindrical

coordinate separately,

$$\nabla^2 E_l(r,z,t) - \frac{1}{c^2} \frac{\partial^2 E_l(r,z,t)}{\partial t^2} = \frac{\omega_p^2(r,z,t)}{c^2} E_l(r,z,t), \quad (8)$$

$$\nabla^2 E_h(r,z,t) - \frac{1}{c^2} \frac{\partial^2 E_h(r,z,t)}{\partial t^2} = \frac{\omega_p^2(r,z,t)}{c^2} E_h(r,z,t) + \mu_0 \frac{\partial^2 P_{nl}(r,z,t)}{\partial t^2}, \quad (9)$$

where

$$\omega_p = e \left[\frac{4\pi n_e(r,z,t)}{m_e} \right]^{1/2} \quad (10)$$

is the plasma frequency, $P_{nl}(r,z,t) = [n_0 - n_e(r,z,t)] d_{nl}(r,z,t)$ is the nonlinear polarization of the medium, n_0 is the gas density, and $n_e(t) = n_0 [1 - \exp(-\int_{-\infty}^t w(t') dt')]$ is the free-electron density in the gas. Equations (8) and (9) can be numerically solved with the Crank-Nicholson method as described in Ref. [41].

The above theoretical model is sufficient to simulate the HHG in gas medium, while for a deeper insight of the underlying physical mechanism we should analyze the phase matching of generated harmonics. The phase matching refers to the constructive accumulation of radiation from coherent sources along the beam propagation direction. The condition of optimum phase matching in the HHG process is $k_q = qk_1$, where k_q is the q th harmonic wave vector and k_1 is the fundamental field wave vector. Since HHG is a highly nonlinear process, both the single-atom response and the macroscopic effects could cause the phase mismatching of the harmonica. The phase mismatching degree can be expressed as [42]

$$\Delta k = \Delta k_g + \Delta k_d + \Delta k_e + \Delta k_a, \quad (11)$$

where $\Delta k_g = q \frac{2}{b[1+(2z/b)^2]}$ results from the spatial phase variations arising from the focusing geometry of the driving laser field, q is the harmonic order, b is the confocal parameter of the beam, z is the position of the medium, and $z < 0$ and > 0 mean the upstream and downstream of the laser focus. $\Delta k_d = \alpha_j \frac{d(U_p/w)}{dz}$ is the phase mismatching due to the intensity-dependent single-atom dipole phase, and α_j is the phase coefficient with $j = S, L$ representing the short and long paths, respectively. $U_p \propto I/\omega^2$ is the ponderomotive energy and ω is the frequency of the driving pulse. $\Delta k_e = \frac{w}{c} \Delta n_{el}(w)$ and $\Delta k_a = \frac{w}{c} \Delta n_{at}(w)$ are due to the dispersions of the free electrons and neutrals, $\Delta n(w)$ is the difference in the refractive index. In this equation, Δk_g and Δk_a are positive and Δk_e is negative. The sign of Δk_d is generally not fixed: when $z < 0$, it is positive; when $z > 0$, it is negative.

III. RESULTS AND DISCUSSION

In this section, we first investigate the individual contributions of the four terms $\Delta k_d, \Delta k_e, \Delta k_a$, and Δk_g to the phase mismatching of HHG. In our simulation, we adopt a 40-fs, 800-nm Gaussian laser field with an intensity of 3.5×10^{14} W/cm². The beam waist of the driving field at the focus is 30 μ m and the medium gas (argon) is placed at $z = -1$ mm. Here, the 15th harmonic is taken as an

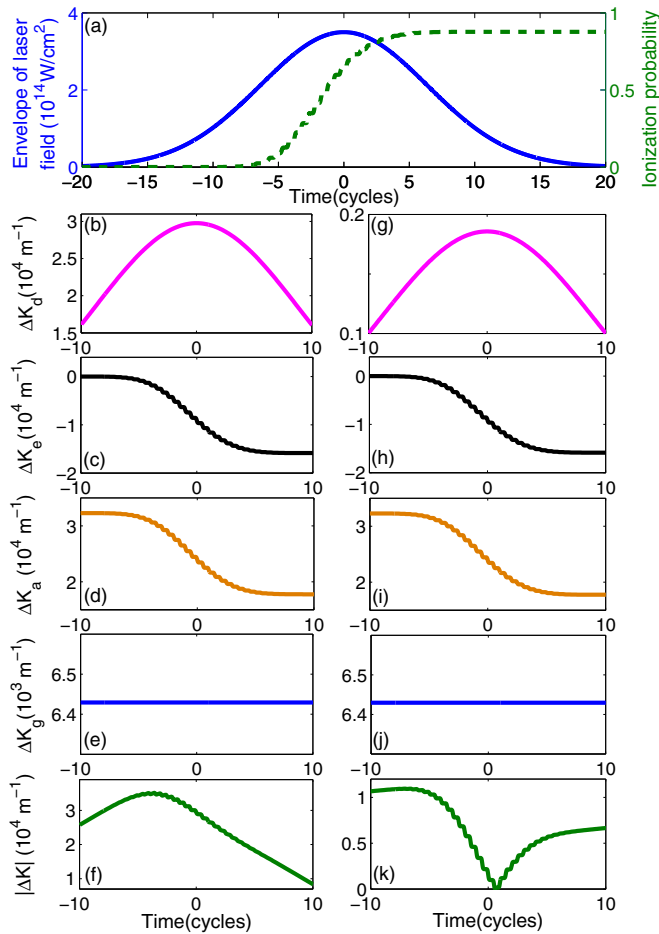


FIG. 1. (Color online) (a) The envelope of the laser field (solid line) and the ionization probability (dashed line). (b)–(f) The on-axis phase-mismatching values of Δk_d , Δk_e , Δk_a , Δk_g , and $|\Delta k|$ of the 15th harmonic for the long path. (g)–(k) Same as (b)–(f), but for the short path. Here, the laser pulse is 40 fs and the laser intensity is 3.5×10^{14} W/cm². The beam waist of the driving field at the focus is 30 μ m and the gas medium is placed at $z = -1$ mm.

example. Figure 1(a) shows the envelope of the laser field (solid line) and the ionization probability (dashed line). With the time increases, the laser field shows a symmetric distribution and the ionization probability increases monotonically. Figures 1(b)–1(f) show the on-axis phase-mismatching values of Δk_d , Δk_e , Δk_a , Δk_g , and $|\Delta k|$ for the long path, respectively. Since the single-atom dipole phase term Δk_d is proportional to dI/dz , it presents a symmetric distribution in time as shown in Fig. 1(b). The contributions of the free electrons and neutrals to phase mismatching can be treated similarly; they both intensively depend on the ionization probability. As the ionization probability increases with time, the densities of the free electrons increase while the densities of the neutrals decrease. Therefore, the negative term Δk_e [Fig. 1(c)] and the positive term Δk_a [Fig. 1(d)] both decrease monotonically. Figure 1(e) shows the geometric term Δk_g , which keeps constant as the time increases. The total phase mismatching $|\Delta k|$ of the long path is presented in Fig. 1(f). One can see that when $t < -5T_0$ (T_0 is the optical cycle of the driving pulse), the laser intensity is not strong enough, the ionization

probability is quite small, and the negative term Δk_e is nearly equal to $0 m^{-1}$. Therefore, phase mismatching is mainly due to the positive terms Δk_g , Δk_a , and Δk_d . Because Δk_d increases with time, $|\Delta k|$ increases with time, too. When $t > -5T_0$, the ionization probability begins to increase rapidly. Then the negative term Δk_e decreases gradually, which compensates the positive terms Δk_g , Δk_d , and Δk_a . As a consequence, $|\Delta k|$ decreases gradually. Figures 1(g)–1(k) show the results for the short path. In Fig. 1(g), Δk_d of the short path also presents a symmetric distribution, but it is much smaller than that of the long path because the phase coefficient is $\alpha_S \ll \alpha_L$. Figures 1(h)–1(j) show the Δk_e , Δk_a , and Δk_g of the short path, which are same to those of the long path. The total phase mismatching $|\Delta k|$ of the short path is shown in Fig. 1(k). One can see that when $t < -5T_0$, $|\Delta k|$ changes very slowly. When $t > -5T_0$, $|\Delta k|$ decreases monotonically. At $t = 0.81T_0$, $|\Delta k|$ is equal to $0 m^{-1}$. This is because the negative term Δk_e is sufficient to compensate the positive terms Δk_g , Δk_d , and Δk_a . When $t > 0.81T_0$, Δk_e overcompensates the positive terms Δk_g , Δk_d , and Δk_a . Then, $|\Delta k|$ turns to increase with time. Above all, the phase mismatching $|\Delta k|$ of the short and long paths vary with time. Moreover, the phase matching at the leading edge of the driving pulse is usually different from that at the falling edge because of the time-dependent ionization yield. For instance, in Fig. 1(f), the long path has a better phase matching at the falling edge, while the optimal phase matching of the short path occurs at $t = 0.81T_0$ as shown in Fig. 1(k). This is very different from the conventional phase-matching model, which leaves out all the time-dependent effects and customarily assumes an optimal phase matching at the center of the laser pulse.

To clarify the above phenomena, we present the distributions of the on-axis $|\Delta k|$ of the 15th harmonic for both the long [Figs. 2(a)–2(c)] and short paths [Figs. 2(d)–2(f)] as a function of time and position of the gas medium. Here, the laser duration is fixed at 40 fs. One can see that the differences of $|\Delta k|$ between the leading and falling edges change gradually as the laser intensity increases. For clarity, we compare the phase-mismatching degrees at two symmetric moments $t = -\tau/2$ (leading edge) and $t = +\tau/2$ (falling edge), where τ is the full width at half maximum. In our comparison, we assume the gas medium is placed at $z = 0$ mm, where Δk_d is equal to $0 m^{-1}$ for both the short and long paths and therefore the $|\Delta k|$ of the short and long paths are the same. At a low laser intensity of 0.5×10^{14} W/cm² [Figs. 2(a) and 2(d)], $|\Delta k|$ is about $11,720.04 m^{-1}$ at $t = -\tau/2$, which is nearly equal to that ($\approx 11,720.00 m^{-1}$) at $t = +\tau/2$. In this case, the phase matching degrees at the leading and falling edges are comparable. When the laser intensity increased to 2.0×10^{14} W/cm² [Figs. 2(b) and 2(e)], the $|\Delta k|$ is approximately equal to $11,710.02 m^{-1}$ at $t = -\tau/2$, while it is only $6749.04 m^{-1}$ at $t = +\tau/2$. Namely, the harmonic emission at the falling edge is better phase matched than the leading edge. On the contrary, as the intensity further increased to 3.5×10^{14} W/cm² [Figs. 2(c) and 2(f)], $|\Delta k|$ at the leading edge ($\approx 11,310.00 m^{-1}$ at $t = -\tau/2$) is smaller than the falling edge ($\approx 21,990.02 m^{-1}$ at $t = +\tau/2$).

On the other hand, the phase matching in the propagation process is usually coupled with the single-atom response. On the single-atom level, the variation of the dipole phase with

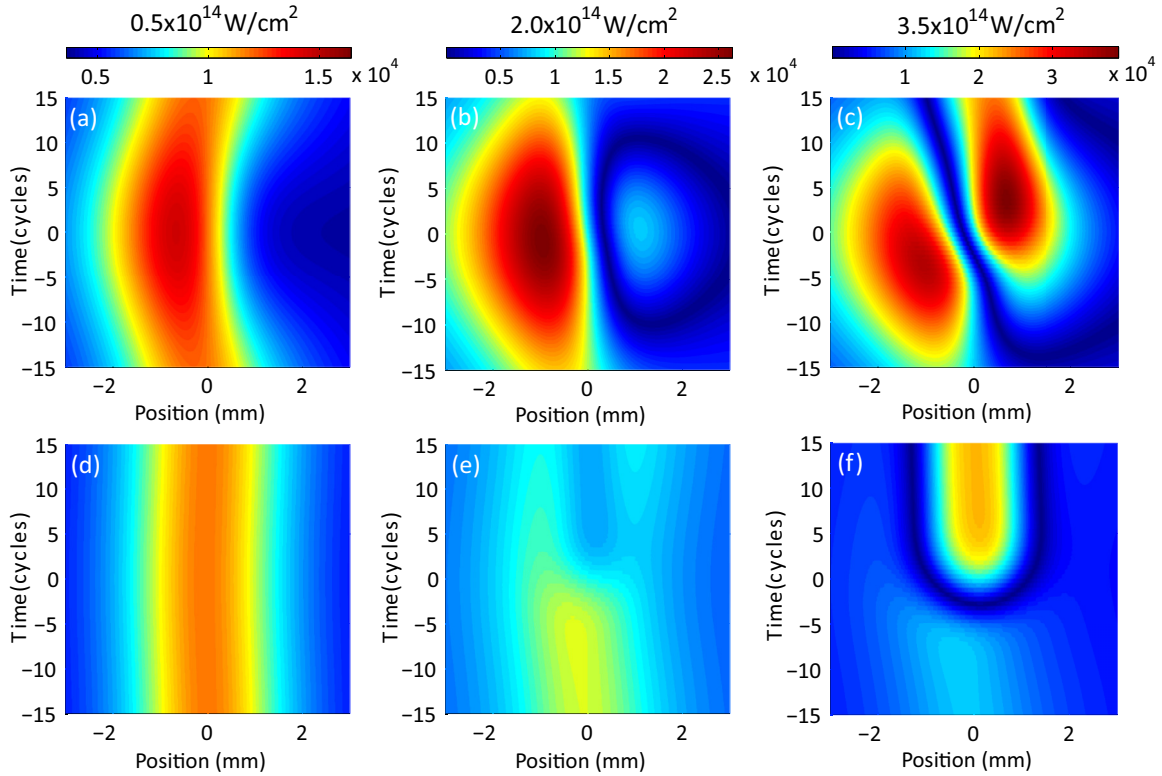


FIG. 2. (Color online) (a)–(c) The on-axis phase mismatching $|\Delta k|$ of the 15th harmonic for the long path with a laser intensity of 0.5×10^{14} W/cm², 2.0×10^{14} W/cm², 3.5×10^{14} W/cm², respectively. (d)–(f) Same as (a)–(c), but for the short path. Blue (red) areas correspond to good (poor) phase matching. Other parameters are the same as in Fig. 1.

time leads to the variation of the instantaneous harmonic frequency, which can be expressed by $\omega_q(t) = q\omega + \alpha_q \partial I(t)/\partial t$ [18,43]. From this equation, one can see that the frequency shifts for the long and short paths depend on the time: at the leading edge of the driving pulse [$\partial I(t)/\partial t > 0$], both the long and short paths present a blueshift, while at the falling edge [$\partial I(t)/\partial t < 0$], it is a redshift. Moreover, the phase-matching degrees of these quantum paths are also time dependent. Thus it will lead to complex spatial structures in harmonic spectra.

To illustrate the impact of the phase matching on the spatial structures of HHG spectra, we simulate the spatially resolved harmonic spectra by solving Maxwell's equations with the method presented in Sec. II. Four laser intensities are adopted: 0.5×10^{14} W/cm² [Fig. 3(a)], 2.0×10^{14} W/cm² [Fig. 3(c)], 2.3×10^{14} W/cm² [Fig. 3(e)], and 3.5×10^{14} W/cm² [Fig. 3(g)]. The corresponding on-axis phase mismatching $|\Delta k|$ of the 15th harmonic for the long path is also presented in Figs. 3(b), 3(d), 3(f), and 3(h). Here, the gas medium is placed at $z = 0$ mm. Note that the frequency shift of the short path is much smaller than that of the long path. In the following, we focus on the harmonic emission from the long path. For a laser intensity of 0.5×10^{14} W/cm², the distribution of $|\Delta k|$ is nearly symmetric in time, as shown in Fig. 3(b). The phase-matching degrees of the long path at the leading and falling edges of the driving pulse are analogous. Figure 3(a) shows the spatially resolved harmonic spectrum. Since the intensity is low, the 15th harmonic is close to the cutoff region, where the short and long paths nearly overlap. To help the eye, the long path of the 15th

harmonic is marked by the dashed ring, which has a large divergence angle for better phase matching. The red spot at the center of the ring corresponds to the short path, which has a small divergence angle. As the intensity increases to 2.0×10^{14} W/cm², $|\Delta k|$ decreases gradually with time [Fig. 3(d)]. The harmonic emission from the long path is more effectively phase matched at the falling edge than the leading edge of the driving pulse. Therefore the splitting structure of each individual harmonic from the long path is dominated by the redshifted component [as shown in Fig. 3(c)]. Moreover, the long path shows a larger divergence angle than the short path. For the intensity of 2.3×10^{14} W/cm², $|\Delta k|$ also presents a symmetric distribution in time [Fig. 3(f)]. This feature is similar to Fig. 3(b). But in the case of Fig. 3(f), the higher laser intensity leads to a larger frequency shift compared with Fig. 3(b). Then the harmonic emission from the long path presents both redshifts and blueshifts simultaneously, as shown in Fig. 3(e). As the intensity is further increased to 3.5×10^{14} W/cm², the values of $|\Delta k|$ at the leading edge are smaller than the falling edge and the optimal phase matching occurs at $t = -2.76 T_0$ (leading edge) [Fig. 3(h)]. Therefore, the long path shows a blueshift in the splitting structure of the HHG spectra [Fig. 3(g)].

Figure 4 shows the spatially integrated harmonic spectra as a function of the laser intensity. One can see clear splitting structures in the HHG spectra. As discussed above, the center peak corresponds to the short path, which presents a very small frequency shift. On the contrary, the side peaks come from the contribution of the long path and present either

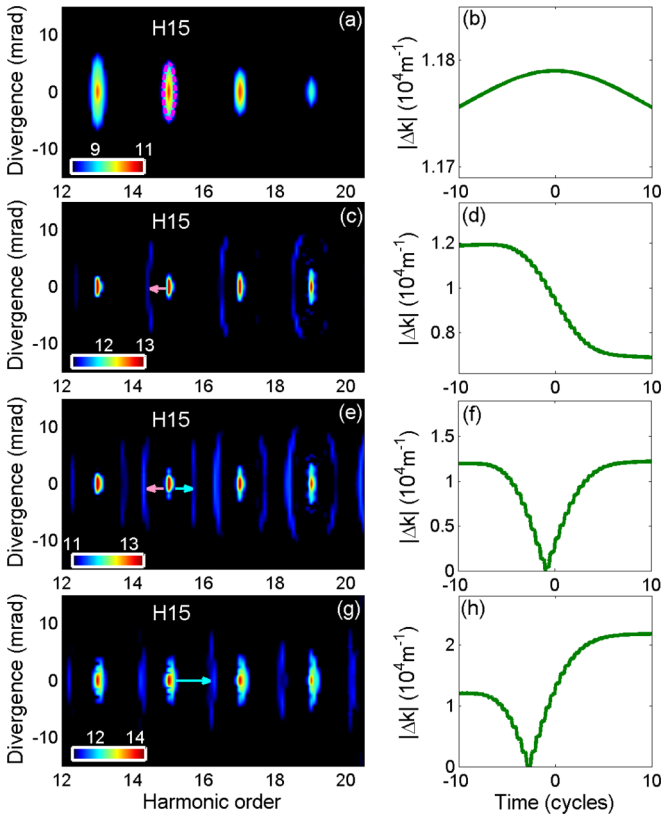


FIG. 3. (Color online) (a) Spatially resolved harmonic spectrum with a laser intensity of 0.5×10^{14} W/cm². (b) The corresponding on-axis phase mismatching $|\Delta k|$ of the 15th harmonic for the long path. (c)–(h) Same as (a),(b), but for an intensity of 2.0×10^{14} W/cm², 2.3×10^{14} W/cm², 3.5×10^{14} W/cm², respectively. Here, the gas medium is placed at $z = 0$ mm. Other parameters are the same as in Fig. 2.

a blue- or a red-frequency shift. At a low laser intensity (below about 1.0×10^{14} W/cm²), $\partial I/\partial t$ is very small and the frequency shift of the side peaks is difficult to observe. When the laser intensity is above 1.0×10^{14} W/cm², the

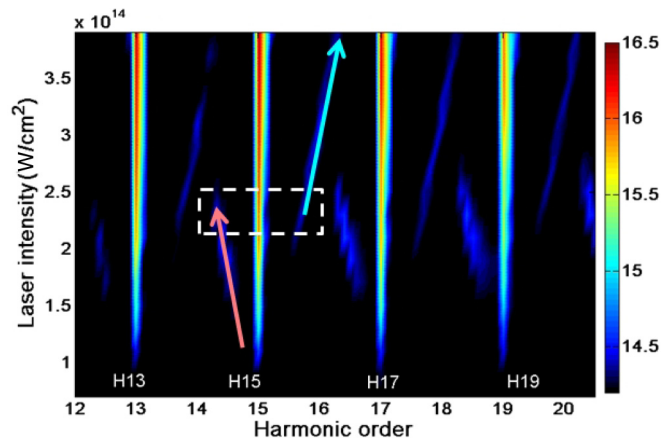


FIG. 4. (Color online) Spatially integrated harmonic spectrum as a function of the laser intensity. Here, the parameters are the same as in Fig. 3.

harmonic emission from the long path begins to present a redshift, which becomes larger as the laser intensity increases (red line with an arrow). The region from 2.1×10^{14} W/cm² to 2.5×10^{14} W/cm² (white dashed rectangle) is a transition area where both the redshifts and blueshifts can be observed simultaneously. As the laser intensity is further increased, the side peaks show only a blueshift, which also increases with the laser intensity (blue line with an arrow). Furthermore, we also calculate the evolution of intensity-dependent harmonic emission at different laser durations. The results show that at different laser durations, the evolutions of intensity-dependent harmonic emission are similar, but the transition areas are different. For example, with a laser duration of 20 fs, the transition area is in the vicinity of the laser intensity of 3.5×10^{14} W/cm², while for a laser duration of 60 fs, it is in the vicinity of 1.0×10^{14} W/cm².

On the other hand, the phase matching of HHG depends on the position of the gas medium. As can be seen in Fig. 2(b), when the gas medium is placed at $z = 0$ mm, $|\Delta k|$ at the leading edge is larger than the falling edge of the driving pulse. Nevertheless, as the gas medium moved away from the focus point, the difference of $|\Delta k|$ between the leading and falling edges is reduced.

In Fig. 5, we simulate the spatially resolved harmonic spectra by placing the gas medium at $z = -2$ mm [Fig. 5(a)] and $z = 2$ mm [Fig. 5(c)]. The corresponding $|\Delta k|$ of the long path at $R = 0$ μ m (on axis) and $R = 20$ μ m (off axis) are shown in Figs. 5(b) and 5(d). The other parameters are the same as Figs. 3(c) and 3(d). One can see that when the gas medium is located at $z = -2$ mm, the distributions of the off-axis and on-axis $|\Delta k|$ are basically symmetric in time. Moreover, the off-axis $|\Delta k|$ (dashed line) values are much smaller than the on-axis $|\Delta k|$ (solid line) [Fig. 5(b)]. Therefore, the harmonic emission from the long path shows a ring structure (marked by the dashed ring), of which the off-axis components are much brighter than the on-axis components, as shown in Fig. 5(a).

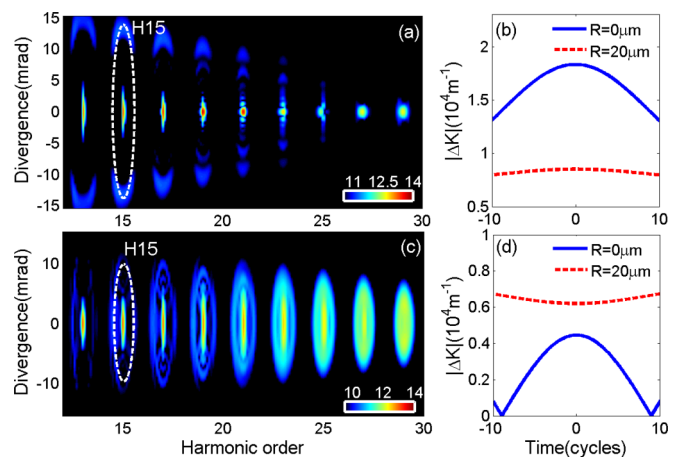


FIG. 5. (Color online) (a),(b) Spatially resolved harmonic spectrum and the corresponding on-axis (solid line) and off-axis (dashed line) phase mismatching $|\Delta k|$ of the 15th harmonic for the long path with a laser intensity of 2.0×10^{14} W/cm² and the gas medium placed at $z = -2$ mm. (c),(d) Same as (a),(b), but the gas medium is placed at $z = 2$ mm. Other parameters are the same as in Figs. 3(c) and 3(d).

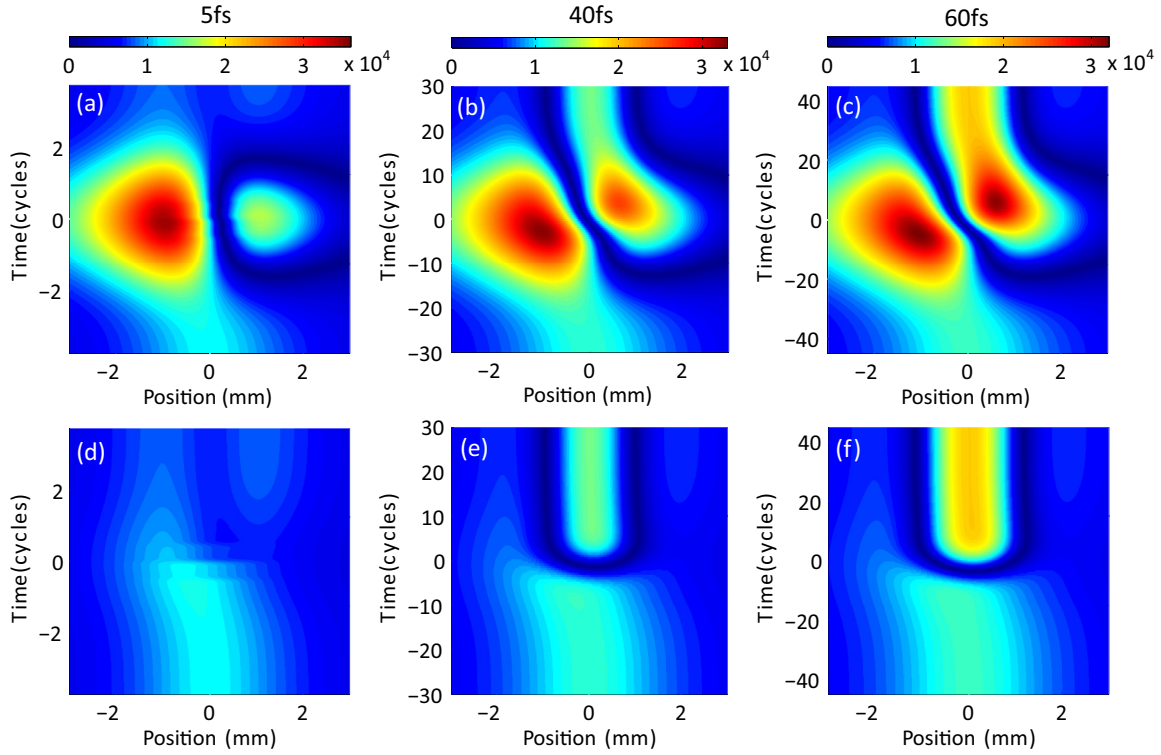


FIG. 6. (Color online) (a)–(c) The on-axis phase mismatching $|\Delta k|$ of the 15th harmonic for the long path with a laser duration of 5 fs, 40 fs, and 60 fs, respectively. (d)–(f) Similar to (a)–(c), but for the short path. Here, the laser intensity is 3.0×10^{14} W/cm². Other parameters are the same as in Fig. 2.

When the medium is placed at $z = 2$ mm, the on-axis and off-axis $|\Delta k|$ are also nearly symmetric in time. But, unlike that in Fig. 5(b), the difference of $|\Delta k|$ between the off axis and on axis is much smaller in Fig. 5(d). Therefore, the harmonic strengths of the off-axis and on-axis components of the ring structure (marked by the dashed ring) are comparable [Fig. 5(c)].

Next, we discuss the influence of the laser duration on the phase matching of HHG. Figures 6(a)–6(c) show the on-axis $|\Delta k|$ of the long path with a laser duration of 5 fs, 40 fs, and 60 fs, respectively. Figures 6(d)–6(f) are the results of the short path. Here, the laser intensity is 3.0×10^{14} W/cm². In the same way, we compare the phase-mismatching degrees at two symmetric moments $t = -\tau/2$ (leading edge) and $t = +\tau/2$ (falling edge) with the medium placed at $z = 0$ mm. As in Fig. 2, the $|\Delta k|$ of the short and long paths are equal at $z = 0$ mm. The results show that for a short laser duration of 5 fs [Figs. 6(a) and 6(d)], $|\Delta k|$ at the leading edge is larger than the falling edge of the driving pulse. Nevertheless, with a laser duration of 40 fs [Figs. 6(b) and 6(e)] and 60 fs [Figs. 6(c) and 6(f)], $|\Delta k|$ at the leading edge is smaller than the falling edge. But for a laser duration of 60 fs, the difference of $|\Delta k|$ between the leading and falling edges is larger.

In Fig. 7, we calculate the spatially resolved harmonic spectra with a laser duration of 20 fs [Fig. 7(a)], 28 fs [Fig. 7(c)], and 60 fs [Fig. 7(e)]. The corresponding on-axis $|\Delta k|$ of the long path are presented in Figs. 7(b), 7(d), and 7(f). Here, the gas medium is placed at $z = 0$ mm. Other parameters are the same as in Fig. 6. One can see that for a laser duration of 20 fs, the values of $|\Delta k|$ at the leading edge are larger than

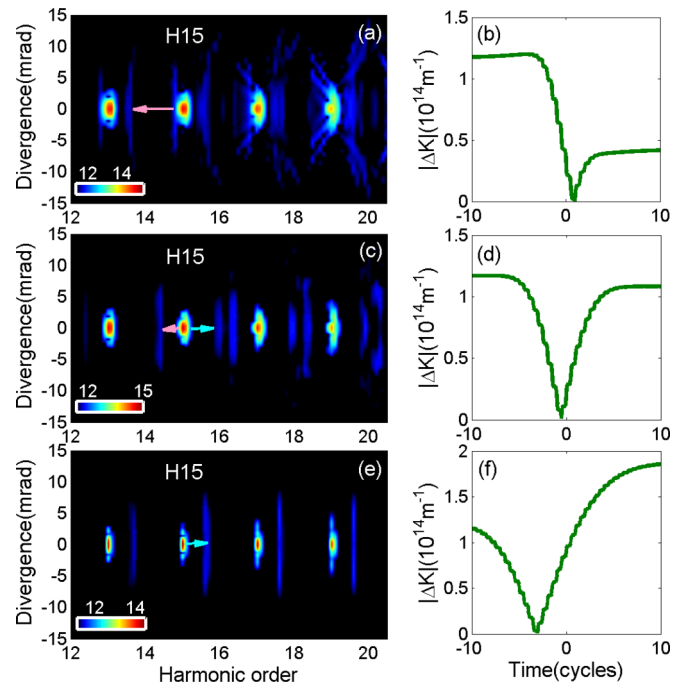


FIG. 7. (Color online) (a) Spatially resolved harmonic spectrum with a laser duration of 20 fs. (b) The corresponding on-axis phase mismatching $|\Delta k|$ of the 15th harmonic for the long path. (c)–(f) Same as (a),(b), but for laser durations of 28 fs, 60 fs, respectively. Here, the gas medium is placed at $z = 0$ mm. Other parameters are the same as in Fig. 6.

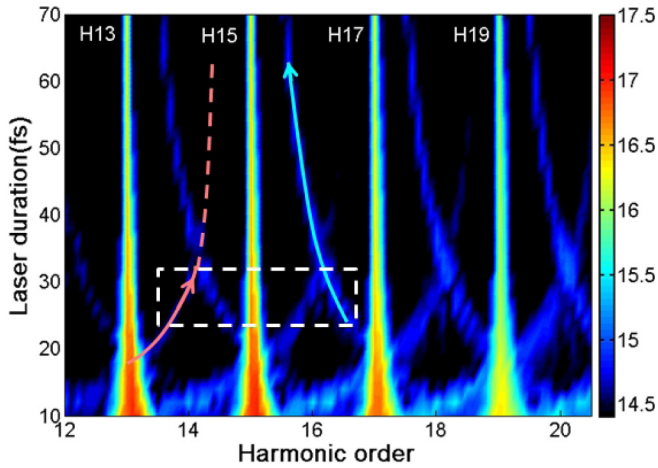


FIG. 8. (Color online) Spatially integrated harmonic spectrum as a function of the laser duration. The parameters are the same as in Fig. 7.

the falling edge, and the optimal phase matching occurs at $t = 1.02 T_0$ (falling edge) [see Fig. 7(b)]. As a consequence, the harmonic emission from the long path presents a redshift as shown in Fig. 7(a). In this case, $\partial I/\partial t$ is very large and the redshift is very large, too. As the laser duration increases to 28 fs, the distribution of $|\Delta k|$ is nearly symmetric in time [Fig. 7(d)]. Therefore, the harmonic emission from the long path shows a redshift and blueshift simultaneously, as shown in Fig. 7(c). In Fig. 7(f) with a laser duration of 60 fs, one can see that the harmonic emission from the long path has a better phase matching at the leading edge than the falling edge of the driving pulse. As a consequence, the long path presents a blueshift in the splitting structure of the HHG spectra [Fig. 7(e)].

Figure 8 shows the spatially integrated harmonic spectra as a function of the laser duration. Similar to Fig. 4, in the splitting structure of the HHG spectra, the center peak corresponds to the short path and the side peaks represent the long path. One can see that when the laser duration is less than 23 fs, the long path first presents a redshift, which gradually decreases with the laser duration (red line with an arrow). The region from 23 fs to 32 fs is a transition area (white dashed rectangle) in which both the redshift and blueshift for the long path can

be observed simultaneously. When the laser duration is larger than 32 fs, the long path shows only a blueshift, which also gradually decreases with the laser duration (blue line with an arrow). Furthermore, we also calculate the evolution of the duration-dependent harmonic emission with different laser intensities. The results show that the evolutions of the duration-dependent harmonic emission are similar at different laser intensities, but the transition areas are different. For example, with the intensity of $2.0 \times 10^{14} \text{ W/cm}^2$, the transition area is in the vicinity of the laser duration of 100 fs, while with the intensity of $4.0 \times 10^{14} \text{ W/cm}^2$, it is in the vicinity of 10 fs.

IV. CONCLUSION

In conclusion, we have theoretically investigated the influence of time-dependent phase matching on HHG. The results show that the phase-matching degrees of the short and long paths are different at the leading and falling edges of the driving pulse due to the ionization effect. It is very different from the conventional phase-matching model, which leaves out all the time-dependent effects. Moreover, the time-dependent phase matching coupled with the single-atom response can lead to harmonic splitting with either a blue- or red-frequency shift in the HHG spectra. The influence of laser parameters on the spatio-spectral properties of the HHG spectra has also been studied. As the laser intensity or duration increases, the harmonic emission from the long path first presents a redshift, then the redshift and blueshift coexist in a transition area, and further it shows a blueshift. The frequency shift increases gradually when the laser intensity is increased or the laser duration is decreased. In addition, the harmonic splitting with either blue- or red-frequency shift can also be observed by changing the position of the gas medium. Our results give a deeper insight and are beneficial for understanding the spatio-spectral features of HHG.

ACKNOWLEDGMENTS

This work was supported by the National Natural Science Foundation of China under Grants No. 61275126 and No. 11234004. Numerical simulations presented in this paper were carried out using the High Performance Computing experimental test bed in SCTS/CGCL.

-
- [1] A. McPherson *et al.*, *J. Opt. Soc. Am. B* **4**, 595 (1987).
 [2] I. P. Christov, M. M. Murnane, and H. C. Kapteyn, *Phys. Rev. Lett.* **78**, 1251 (1997).
 [3] P. Lan, P. Lu, W. Cao, Y. Li, and X. Wang, *Phys. Rev. A* **76**, 051801 (2007); J. Luo, Y. Li, Z. Wang, Q. Zhang, and P. Lu, *J. Phys. B* **46**, 145602 (2013).
 [4] Z. Chang, A. Rundquist, H. Wang, M. M. Murnane, and H. C. Kapteyn, *Phys. Rev. Lett.* **79**, 2967 (1997).
 [5] G. Sansone, E. Benedetti, F. Calegari, C. Vozzi, L. Avaldi, R. Flammini, L. Poletto, P. Villoresi, C. Altucci, R. Velotta, S. Stagira, S. De Silvestri, and M. Nisoli, *Science* **314**, 443 (2006).
 [6] Y. Zhou, C. Huang, Q. Liao, and P. Lu, *Phys. Rev. Lett.* **109**, 053004 (2012); A. Tong, Y. Zhou, and P. Lu, *Opt. Express* **23**, 15774 (2015); Y. Li, P. Lan, H. Xie, M. He, X. Zhu, Q. Zhang, and P. Lu, *ibid.* **23**, 28801 (2015).
 [7] R. Kienberger *et al.*, *Science* **297**, 1144 (2002).
 [8] M. Li, P. Zhang, S. Luo, Y. Zhou, Q. Zhang, P. Lan, and P. Lu, *Phys. Rev. A* **92**, 063404 (2015); Q. Liao, Y. Zhou, C. Huang, and P. Lu, *New J. Phys.* **14**, 013001 (2012); C. Huang, Y. Zhou, Q. Zhang, and P. Lu, *Opt. Express* **21**, 11382 (2013).
 [9] J. Itatani *et al.*, *Nature (London)* **432**, 867 (2004).
 [10] Y. Li, X. Zhu, P. Lan, Q. Zhang, M. Qin, and P. Lu, *Phys. Rev. A* **89**, 045401 (2014).

- [11] S. Baker *et al.*, *Science* **312**, 424 (2006).
- [12] P. B. Corkum, *Phys. Rev. Lett.* **71**, 1994 (1993).
- [13] C. Vozzi, M. Negro, F. Calegari, S. Stagira, K. Kovács, and V. Tosa, *New J. Phys.* **13**, 073003 (2011).
- [14] M. Chini, X. Wang, Y. Cheng, H. Wang, Y. Wu, E. Cunningham, P. Li, J. Heslar, D. A. Telnov, S. Chu, and Z. Chang, *Nat. Photonics* **8**, 437 (2014).
- [15] C. Jin, A. T. Le, C. A. Trallero-Herrero, and C. D. Lin, *Phys. Rev. A* **84**, 043411 (2011).
- [16] M. B. Gaarde, J. L. Tate, and K. J. Schafer, *J. Phys. B* **41**, 132001 (2008).
- [17] V. Tosa, H. T. Kim, I. J. Kim, and C. H. Nam, *Phys. Rev. A* **71**, 063808 (2005).
- [18] P. Salières, A. L’Huillier, P. Antoine, and M. Lewenstein, *Adv. At., Mol., Opt. Phys.* **41**, 83 (1999).
- [19] S. C. Rae, K. Burnett, and J. Cooper, *Phys. Rev. A* **50**, 3438 (1994).
- [20] P. Antoine, A. L’Huillier, and M. Lewenstein, *Phys. Rev. Lett.* **77**, 1234 (1996).
- [21] J. Peatross and D. D. Meyerhofer, *Phys. Rev. A* **51**, R906 (1995).
- [22] I. Osborne and J. Yeston, *Science* **317**, 765 (2007).
- [23] P. B. Corkum and F. Krausz, *Nat. Phys.* **3**, 381 (2007).
- [24] M. Hentschel, R. Kienberger, C. Spielmann, G. A. Reider, N. Milosevic, T. Brabec, P. Corkum, U. Heinzmann, M. Drescher, and F. Krausz, *Nature (London)* **414**, 509 (2001).
- [25] M. Uiberacher *et al.*, *Nature (London)* **446**, 627 (2007).
- [26] E. Goulielmakis *et al.*, *Science* **305**, 1267 (2004).
- [27] R. Kienberger *et al.*, *Nature (London)* **427**, 817 (2004).
- [28] C. A. Haworth, L. E. Chipperfield, J. S. Robinson, P. L. Knight, J. P. Marangos, and J. W. G. Tisch, *Nature Phys.* **3**, 52 (2007).
- [29] T. Augustine, P. Salières, A. S. Wyatt, A. Monmayrant, I. A. Walmsley, E. Cormier, A. Zaïr, M. Holler, A. Guandalini, F. Schapper, J. Biegert, L. Gallmann, and U. Keller, *Phys. Rev. A* **80**, 033817 (2009).
- [30] A. Zaïr, M. Holler, A. Guandalini, F. Schapper, J. Biegert, L. Gallmann, U. Keller, A. S. Wyatt, A. Monmayrant, I. A. Walmsley *et al.*, *Phys. Rev. Lett.* **100**, 143902 (2008).
- [31] L. He, P. Lan, Q. Zhang, C. Zhai, F. Wang, W. Shi, and P. Lu, *Phys. Rev. A* **92**, 043403 (2015).
- [32] E. Brunetti, R. Issac, and D. A. Jaroszynski, *Phys. Rev. A* **77**, 023422 (2008).
- [33] J. Jiang, P. Wei, Z. Zeng, J. Miao, Y. Zheng, X. Ge, C. Li, R. Li, and Z. Xu, *Opt. Express* **22**, 15975 (2014).
- [34] X. He, M. Miranda, J. Schwenke, O. Guilbaud, T. Ruchon, C. Heyl, E. Georgadiou, R. Rakowski, A. Persson, M. B. Gaarde, and A. L’Huillier, *Phys. Rev. A* **79**, 063829 (2009).
- [35] C. Corsi, A. Pirri, E. Sali, A. Tortora, and M. Bellini, *Phys. Rev. Lett.* **97**, 023901 (2006).
- [36] A. Dubrouil, O. Hort, F. Catoire, D. Descamps, S. Petit, E. Mével, V. V. Strelkov, and E. Constant, *Nat. Commun.* **5**, 4637 (2014).
- [37] V. Tosa, K. T. Kim, and C. H. Nam, *Phys. Rev. A* **79**, 043828 (2009).
- [38] M. Lewenstein, Ph. Balcou, M. Yu. Ivanov, A. L’Huillier, and P. B. Corkum, *Phys. Rev. A* **49**, 2117 (1994).
- [39] P. Lan, P. Lu, Q. Li, F. Li, W. Hong, and Q. Zhang, *Phys. Rev. A* **79**, 043413 (2009); P. Lan, P. Lu, W. Cao, X. Wang, and G. Yang, *ibid.* **74**, 063411 (2006).
- [40] M. V. Ammosov, N. B. Delone, and V. P. Krainov, *Sov. Phys. JETP* **64**, 1191 (1986).
- [41] E. Priori, G. Cerullo, M. Nisoli, S. Stagira, S. De Silvestri, P. Villoresi, L. Poletto, P. Ceccherini, C. Altucci, R. Bruzzese, and C. de Lisio, *Phys. Rev. A* **61**, 063801 (2000).
- [42] P. Balcou, P. Salières, A. L’Huillier, and M. Lewenstein, *Phys. Rev. A* **55**, 3204 (1997).
- [43] M. B. Gaarde, F. Salin, E. Constant, P. Balcou, K. J. Schafer, K. C. Kulander, and A. L’Huillier, *Phys. Rev. A* **59**, 1367 (1999).